

## **Study of Coronagraphic Techniques**

**Volker Tolls**

*Harvard-Smithsonian Center for Astrophysics, 60 Garden Street, Cambridge, MA 02138*

**Michael J. Aziz**

*Division of Engineering and Applied Sciences, Harvard University, Cambridge, MA 02138*

**Robert A. Gonsalves**

*Tufts University, 161 College Ave., Medford, MA 02155*

**Sylvain Korzennik, Gary Melnick**

*Harvard-Smithsonian Center for Astrophysics, 60 Garden Street, Cambridge, MA 02138*

**Antoine Labeyrie**

*Observatoire de Haute-Provence, 04870 Saint-Michel l'Observatoire, France*

**Richard Lyon**

*NASA/Goddard Space Flight Center, Code 935, Greenbelt, MD 20771*

**Steve Somerstein, Gopal Vasudevan**

*Lockheed Martin Corporation, 3251 Hanover Street, Palo Alto, CA 94304*

**Robert Woodruff**

*Lockheed Martin Corporation, P.O. Box 179, Denver, CO 80201*

### **1. ABSTRACT**

Direct imaging of extra-solar planets is important for determining the properties of individual planets, for studying multi-planet systems, and for observing the spatial structure of debris disks. Obtaining spectra of extra-solar planets enables us to constrain the composition of planetary atmospheres and surfaces, their climates, and their rotation periods. The techniques required to isolate and detect an extra-solar planet next to its host star are quite challenging and require significant improvement. SAO has set up a testbed to study coronagraphic techniques, starting with Labeyrie's multi-step speckle reduction technique.

The testbed consists of a star simulator, an optional planet simulator, a 2-inch spherical mirror with  $\lambda/1000$ -surface quality simulating a telescope, a classical Lyot-coronagraph with high precision optics, and a single step of Labeyrie's speckle reduction method. The Labeyrie correction stage consists of a mirror to relay the light onto a 140-element MEMS deformable mirror (DM) for the phase correction. The reflected light is then focused onto a second occulter to block most of the speckle light and finally imaged onto a CCD. The phase correction function and, thus, the drive signal for the DM, is derived from images taken in and slightly out of the focal plane using phase diversity. The expected performance improvement is about one order of magnitude. An advanced concept utilizing phase and amplitude correction promises an even higher degree of speckle light suppression.

In addition, we are using the testbed to characterize occulter masks developed in collaboration with Harvard University and Lockheed Martin Corporation (LMCO). At Harvard University we are developing a method to shape occulter masks out of dye-doped poly(methyl methacrylate) (PMMA or “Plexiglas”) using a focused ion beam (FIB) system. Using dye-doped PMMA should enable us to manufacture masks that work at any wavelength from the visible (about 500 nm) to the near-infrared (about 1700 nm). It should also be possible to manufacture masks for the IR if a suitable mask material can be found. LMCO is developing occulter masks by creating dot patterns specifically for the desired mask function and transferring these patterns lithographically onto mask substrates. This method will not be described in this paper. In order to test the absorption profile of these masks, we are developing a high-precision mask scanner and employ a maximum entropy algorithm to recover the mask shape.

## 2. MASK DEVELOPMENT

Our project includes two parallel efforts to manufacture soft-edge occulter masks for suppressing the host star light by  $>10^{10}$ . The first program is a cooperative effort between Harvard University and the Smithsonian Astrophysical Observatory, and the second program is at LMCO. The initial Harvard approach was described in [1]. This approach consisted of drilling molds into a Si-carrier followed by filling the mold with absorber material, depositing the absorber onto a glass substrate, and removing the Si-carrier. When milling the first test mold, we discovered that directly shaping the occulter mask out of absorber material will be less complicated, not requiring the steps of filling the mold, planarizing the flat surface of the mask, and transferring the mask onto an optical carrier.

Although there are many possible soft-edge occulter mask shapes, e.g. Gaussian-shaped occulter masks,  $\text{sinc}^2$ -masks[2], and,  $n^{\text{th}}$ -order masks [3], our efforts mostly focus on Gaussian-shaped masks. The primary reason is that the shape of the mask is among the easier shapes with only a central peak and approximating full transparency in the outer mask regions. All other masks include regions of changing transparency over the complete mask aperture. Fig. 1 shows the transmissivity of the earlier mentioned mask types. More important for our development are the mask height functions. These specify the amount of absorber material required to achieve the desired transmissivity profile. For Gaussian-shaped occulter masks, the height function approaches zero thickness at a distance of 8-10  $\lambda/D$  from the center of the mask (or 8-10  $\lambda f/D$  in physical units with  $\lambda$  the wavelength of the blocked light,  $f$  the focal length at the occulter and  $D$  the diameter of the beam at the focusing optics). The  $\text{sinc}^2$ -mask shows a more complicated profile. However, we assume that we can still manufacture  $\text{sinc}^2$ -masks if it is possible to cut off the mask profile after a few Airy rings. The 8<sup>th</sup>-order mask profile shown is the most difficult profile to manufacture utilizing the FIB milling approach (see next paragraph) due to the grating-like surface in the outer regions with a thickness of less than 100 nm.

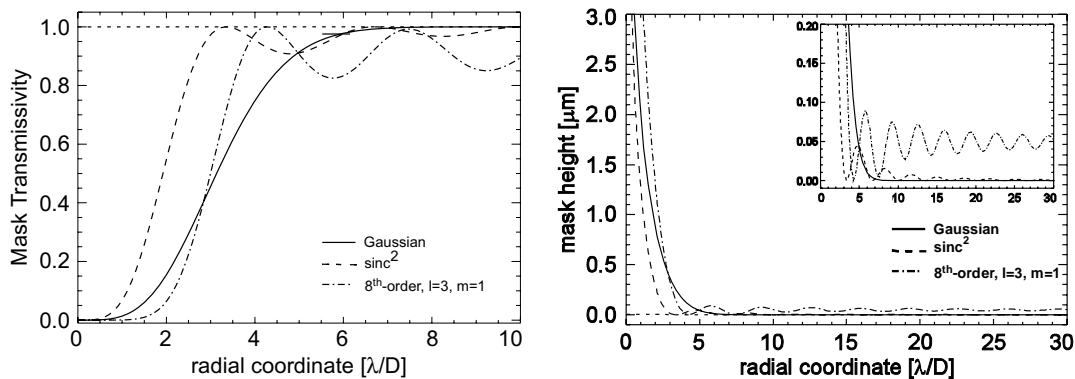


Fig. 1: Absorption profile (right) and profile functions (left) of soft-edge occulter masks: 1) masks with Gaussian-shaped absorption profile (“Gaussian mask”; solid line), 2)  $\text{sinc}^2$  masks (dashed line), and 3) 8<sup>th</sup>-order mask (dash-dot line).

In [1] we have described an occulter mask fabrication method using a focused ion beam (FIB) system. The procedure included milling a shaped mold into a sacrificial substrate followed by filling the mold and removing the substrate.

Alternatively, we are pursuing methods to directly shape absorber material. The direct-milling approach (Fig. 2) starts out with depositing the absorbing mask material onto a transparent substrate as a layer with the desired thickness (e.g. 10  $\mu\text{m}$ ). Then the mask is shaped in three steps: a) a rough out step removes the bulk of the absorber material, b) a precision milling step produces the desired mask profile with a smooth surface, and c) in a final step the mask is embedded in clear dye-free glass. The last step is important for minimizing undesired wavefront changes due to the mask. It can be achieved by embedding the mask in transparent material with matching refractive index.

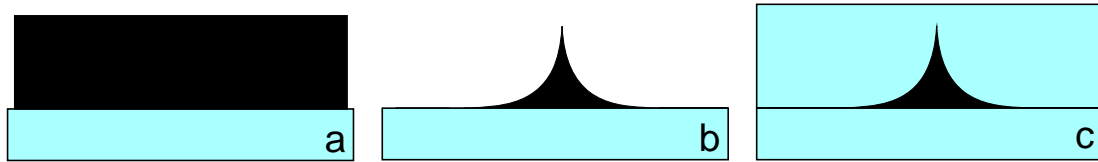


Fig. 2. Fabrication procedure for direct-milled, soft-edge Lyot stops. In (a), the absorbing material (black) is deposited as a layer of known thickness onto the substrate (light blue), (b) then the mask shape (height function) is milled, and (c) the mask is embedded in clear, dye-free glass (also light blue).

A recent test result of the direct-milling approach is shown in Fig. 3. The image shows a scanning electron microscope (SEM) picture of a shaped cone manufactured using an overlapping annulus method. The FIB created the cone by moving in overlapping concentric circles with varying radii around the center of the mask. The amount of removed material was controlled through appropriate changes of the exposure time. The advantage of this method is that it creates very smooth surfaces. There is no surface roughness visible on the central cone. An alternate method would be using a script and exposing a grid of positions with varying exposure times. This method has the advantage that the script can be computer generated. However, the disadvantage is that the surface is not as smooth as using the annulus method.

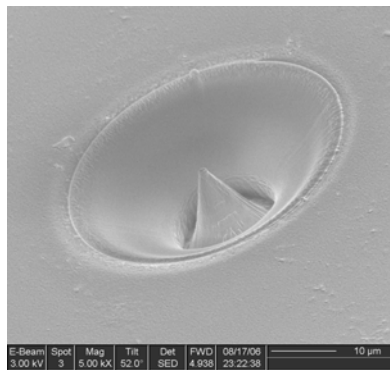


Fig. 3. Results from FIB manufacturing tests performed by Shilpa N. Raja as part of a Harvard-DEAS Research Experience for Undergraduate (REU) program ([4]). The SEM-picture shows a direct-milled absorber cone. The material is PMMA doped with Oilblack BT dye.

Potential dyes for doping PMMA to manufacture masks at visible wavelengths (550 nm to 850 nm) are Oilblack BT and BASF IR dye. The optical densities for both materials are  $\sim 1\mu\text{m}^{-1}$  [5]. This means that the mask must be at least 10  $\mu\text{m}$  thick in the center in order to reach a suppression of  $10^{10}$  of the incoming light. Currently, we are also investigating dyes from Epolin Inc. for near-infrared wavelengths (850 nm to 1100 nm).

### 3. MASK SIMULATIONS

In order to better understand and correct phase effects and possible performance deviation, we have developed software that applies the beam propagation method (bpm) on non-planar masks. This method was introduced [6] to simulate the light propagation through optical fibers. Fig. 4 shows the result of an ideal wave with Airy pattern traveling from the left to the right through an ideal Gaussian-shaped occulter. The intensities in the plot are color coded from black to white (smallest to largest) and are displayed on a logarithmic scale. The attenuation of the light by the mask can clearly be seen in the middle of the left side. The mask has a thickness of about  $10\ \mu\text{m}$  and its central peak ends about where the blue horizontal cone in the plot starts. The horizontal blue stripes indicate where the intensity of the incoming beam is zero. For the case that the refractive index of the absorber material is larger than the refractive index of the surrounding material, the mask acts like a positive lens. Further improvements of this method include testing variations of the bpm method; modeling measured mask shapes; introducing surface errors on the mask; testing tip, tilt, and other effects; and possibly expanding the simulation using a full vector simulation (bpm is a scalar method).

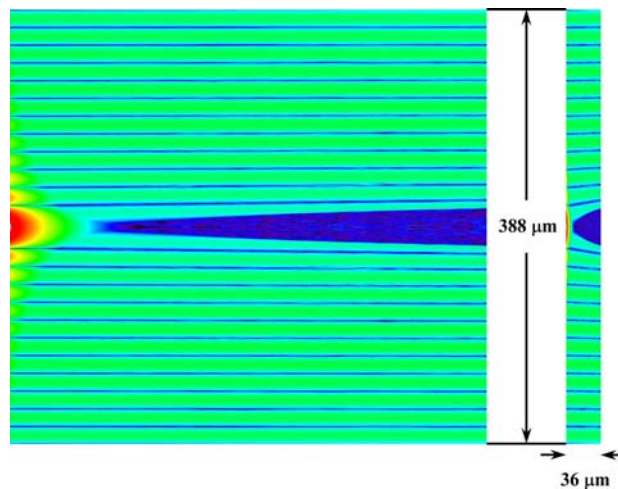


Fig. 4: Example of a beam propagation method simulation. An occulter with Gaussian absorption profile is illuminated by an ideal wave. The left picture is stretched in the propagation direction (horizontally), whereas the right picture shows the same data with the correct aspect ratio. For further explanation, see the text above.

### 4. MASK SCANNER

After manufacturing the mask, it is very important to measure the mask performance with optical methods. The FIB system includes a surface electron microscope with which the physical size of the mask can be measured. However, it cannot measure the shape of the mask. In order to obtain the transmission profile of the mask and, thus, to predict the occulter's performance, we have designed a mask scanner.

The mask scanner (see Fig. 5) consists of a laser light source, collimating optics, mask holder mounted on an x- and y-translation stage, pinhole, detector, and control electronics. The He-Ne laser beam is focused to a spot size of about  $1\ \mu\text{m}$  using 14.5 mm focal length collimating optics from Melles Griot. The clearance between the collimating optics and the mask under test is only 3 mm. The location of the focal spot is in the mask plane which is perpendicular to the optical axis of the tester. The occulter mask under test is mounted on an x- and y-translation stage. The Newport XPS-translation stage can be moved with 50 nm repeatability over a 25-mm range in x- and y-direction (the optical axis is the z-direction). This enables us to scan up to 1-inch by 1-inch masks. The transmitted beam is clipped by a pinhole and the

intensity of the remaining light is measured utilizing a pin diode detector. The dynamic range of the detector is 120 dB, however, it is expected that we cannot utilize the full detector dynamic range due to scattered light and light leakage. We are estimating that the effective dynamic range for the mask measurements is between 60 and 80 dB. The test setup will be computer-controlled to allow synchronous movement of the translation stages and measurements of the transmitted light intensities. A typical measurement will be done in two steps: 1) an initial rough alignment scan to quickly determine the center of the mask (typical mask diameters are less than 1 mm) followed by 2) a fine raster scan of the central mask area. The hardware of the mask scanner is ready and the software will be operational shortly.

Once a mask is scanned, the resulting sampled image is a 2-dimensional spatial convolution of the optical point spread function (PSF) of the scanner with the true mask. We desire to estimate the true mask from the observed sampled and noisy constructed image. This can be performed by using a maximum entropy algorithm [7]. Maximum entropy is a well understood approach for ill-posed inversion problems which attempts to find the least informative solution out of the space of possible solutions. The space of possible solutions is that region of the space for which any linear combination of solutions represents a valid solution due to the ill-posed nature of the problem. It can be shown that the only unbiased solution is that which simultaneously maximizes the entropy and the likelihood.

Fig. 6 shows the result of the maximum entropy algorithm using a simulated mask. The simulated mask is shown in the upper left and the optical point spread function for a laser source is shown in the upper middle and the resultant scanned image at the upper right. The lower right shows the maximum entropy recovered image while the lower middle shows the difference between the true mask and the recovered mask. The plot shows the relative error versus spatial frequency (i.e. error power spectral density of the recovery process). The error is small over the entire range and is very small below the optical cutoff frequency showing that accurate recovery is possible.

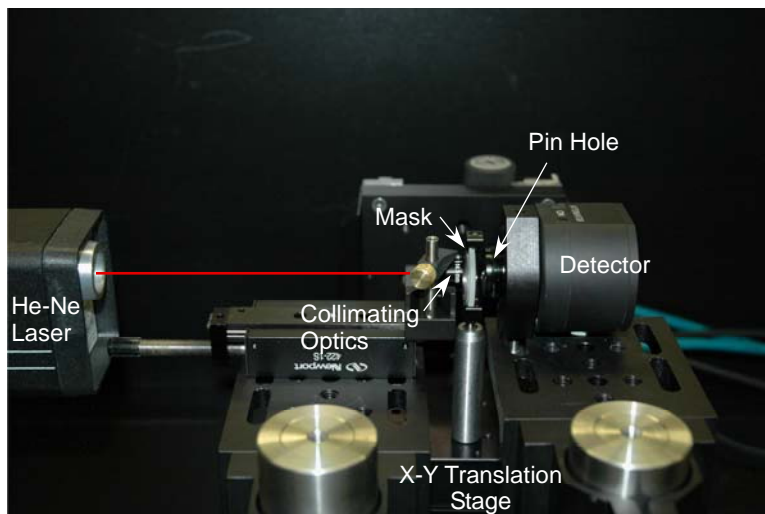


Fig. 5: Schematic (Zemax model) of SAO's mask tester (left) and test setup (right). The He-Ne laser light is focused onto the occulter mask. The transmitted light is then measured through a pinhole using a pin diode detector. The separation between the collimating optics and the mask and between the mask and the pinhole are kept as small as possible to place the focal spot in the mask plane and to collect as much light as possible.

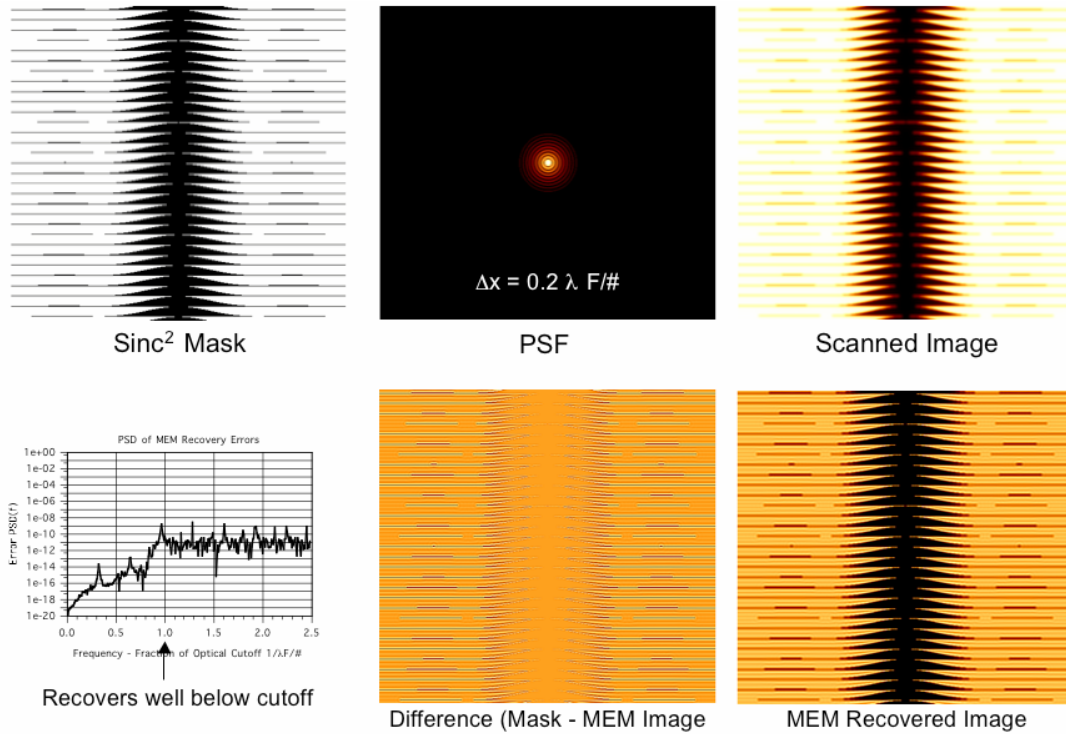


Fig. 6: Simulation of the Maximum Entropy Recovery Process. The scanned image (top right) is the convolution of the mask function (top left) and the PSF of scanner (top middle). The bottom left plot shows the error power spectral density of the recovery process. The recovered image is shown on the bottom right together with the difference to the scanned image (bottom middle). The relative error versus spatial frequency (bottom left) is especially low below the cutoff.

Fig. 7 shows the recovery process for average image signal-to-noise ratios of 10, 100 and 1000. The recovery is relatively poor at SNR = 10, showing a mottled pattern due to the noise. The recovery is better at SNR = 100 but still shows some noise and less sharp edges while at SNR = 1000 the recovery is nearly ideal. The recovery process is acceptable for readily achieved SNR > 200.

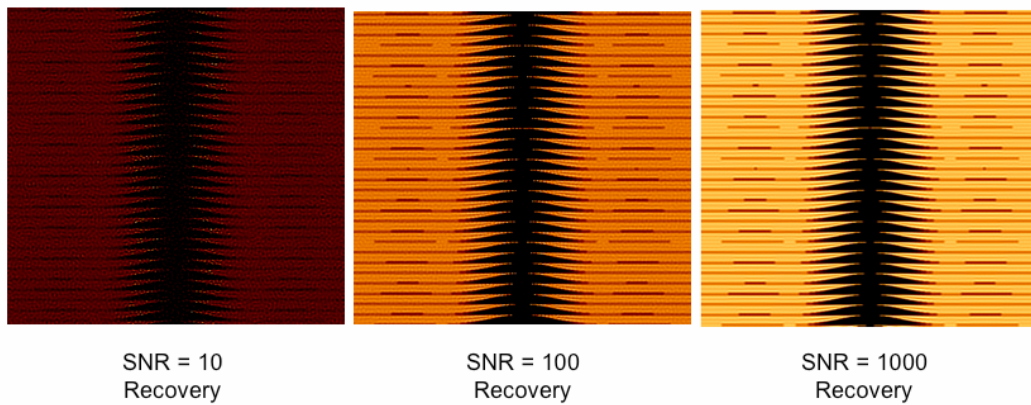


Fig. 7: Maximum Entropy for varying Signal-to-Noise Ratio

## 5. CORONAGRAPHIC TESTBED

SAO's coronagraphic testbed consists of the following elements: 1) the simulated source, 2) the telescope, 3) the Lyot coronagraph, 4) a single stage of Labeyrie's speckle reduction technique, and 5) the camera. Fig. 8 shows a ZEMAX model of the testbed and Fig. 9 shows the testbed during alignment of the coronagraph. The simulated stellar source is a 1 mW He-Ne laser. The output beam is fed into a spatial filter with a 22-mm focal length objective and a 10  $\mu\text{m}$  pinhole. The transmitted light enters the coronagraph uncollimated. The telescope is a 2-inch diameter, spherical mirror (radius is 2 meters to keep spherical aberration negligible) with a surface accuracy of  $\lambda/1000$  at 633 nm from WavePrecision Inc. It is positioned at a distance of about 2 meters from the pinhole. The reflected converging beam passes through an optional apodizer, a cosine function HEBS mask from Canyon materials, and focuses onto the occulting mask. The occulting mask can be a mask manufactured as part of our project or purchased commercially. The mask in Fig. 9 was designed by LMCO. The final elements of the coronagraph are the Lyot stop followed by a 1-inch, 0.5-m radius, spherical mirror with a surface accuracy of  $\lambda/1000$  at 633 nm from WavePrecision Inc. (all following mirrors will be of the same type). In addition to the star simulator laser we can add a second attenuated laser simulating a planet.

The phase correcting element in our single stage Labeyrie speckle corrector is a deformable mirror from Boston Micromachines Inc. This mirror has 140 elements, a 12-by-12 pixel array with the mirrors in the corners missing. The size of a single pixel is 275 x 275  $\mu\text{m}$  with 300  $\mu\text{m}$  spacing and the total array size is 3.3 by 3.3 mm. The stroke per element is 2  $\mu\text{m}$  with 2 nm repeatability. The purpose of this mirror is to correct the phase fronts of the speckle light to achieve a plane wavefront ("re-phasing" the speckle light). Then corrected speckle light can be focused onto a second occulter, effectively eliminating most of the speckle light. It should be noted that we do not expect as high a speckle suppression as the simulation showed since the deformable mirror has a resolution of less than 6 cycles per aperture compared to less than 256 cycles per aperture in the simulation. The final "cleaned" image is focused onto the detector. The detector is an Apogee CCD camera, ST-401. The CCD is the Kodak full-frame CCD KAF-0401E with 768 by 512 pixels of 9 by 9  $\mu\text{m}$  size. The dynamic range at room temperature is 74 dB. The camera is mounted on a translation stage. This enables us to quickly shift the CCD array in and out of the focal plane to take images required for the phase diversity approach. We will use the phase diversity approach, applying a modified Gerchberg-Saxton algorithm, to recover the phase information from these measured images which is required to calculate the response function of the deformable mirror for the phase correction.

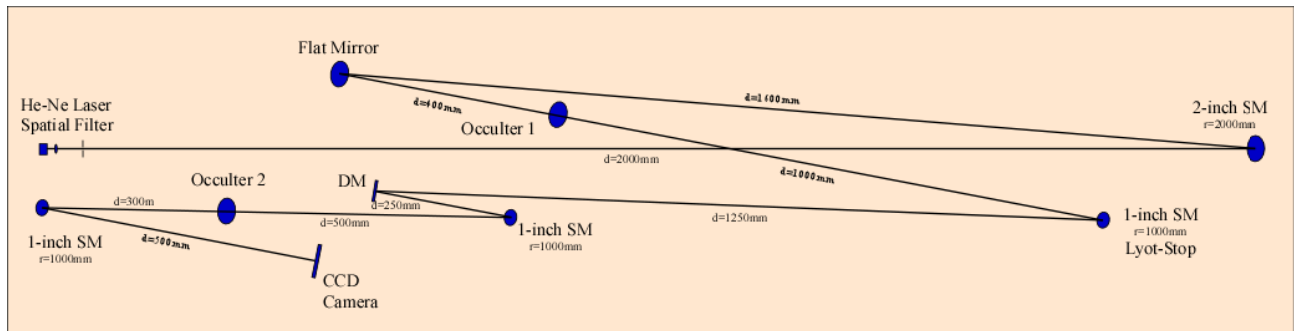


Fig. 8: ZEMAX model of SAO's coronagraphic testbed.

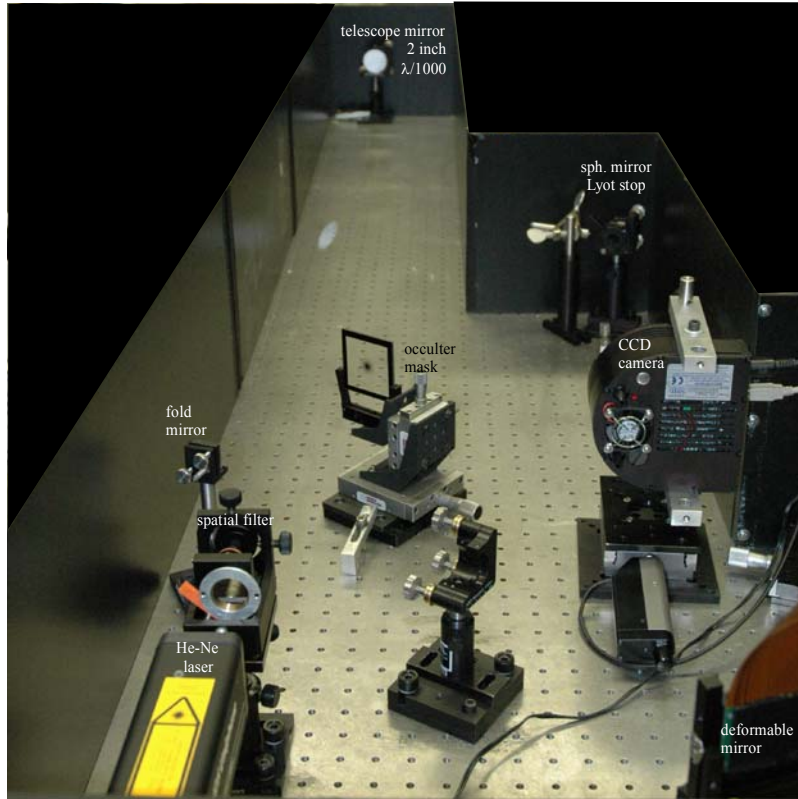


Fig. 9. Picture of SAO's coronagraphic testbed. The testbed consists of a He-Ne laser light source with spatial filter, a 2-inch mirror, an apodizer, a fold mirror, the occulter mask, another spherical mirror with Lyot stop and a Kodak CCD camera (mounted on a translation stage). The speckle reduction step is not included in this setup.

## 6. WAVEFRONT PHASE ESTIMATE

As noted in the previous section, we will use a phase diversity approach to retrieve the phase information of the light passing through our coronagraph in order to calculate a correction signal for the deformable mirror. Phase diversity uses two or more images of an extended object to make a joint estimate of the object itself and the unknown phase front. Its advantage is that it does not require a point source such as a bright star or a laser guide star to estimate the phase and/or the object and that all available energy is used for the estimate of the object.

The procedure for applying phase diversity to derive the DM correction signal is a modified Gerchberg-Saxton (GS) algorithm ([8]): 1) we measure a PSF  $p_1$  in the focal plane and a second PSF  $p_2$  in an out-of-focus plane; 2) we calculate the quadratic phase of  $p_2$ ; 3) we add a random phase (as initial estimate of our pupil phase) to the quadratic phase from 2) to force constraints on  $p_2$  and subtract the quadratic phase of  $p_1$ ; 4) we repeat this procedure by alternating the images at each iteration. The iteration stops when the estimate is good and the difference is small. Then, the residual phase is applied in a clear aperture and the resulting PSF is calculated together with the residual Strehl ratio. If the Strehl ratio reaches 1.0, the iterations are stopped. This algorithm converges reliably when we threshold the PSF: starting only with the highest intensities and lowering the threshold as the iterations progress until the full PSF is revealed.

In the case of our testbed, we apply the described algorithm to find the phase of the speckle pattern that dominates coronagraphic images. Fig. 10 shows simulated images  $p_1$  and  $p_2$  and the phase of  $p_1$  as input for the phase diversity

algorithm and Fig. 11 shows the differences of the phase in Fig. 10 and the estimated phases after 1, 20, and 40 iterations. It can be seen that the differences become increasingly smaller (or darker) starting in the center and moving outwards (due to the thresholding). As a measure for the quality of the recovered phase, we use the spectral Strehl ratio (see [8]). Fig. 12 shows the spectral Strehl ratio versus iteration number for 100 simulations. The algorithm is very reliable, but shows random occasions of slow or no convergence. Future study of this technique is required to reveal the reasons for the slow convergence.

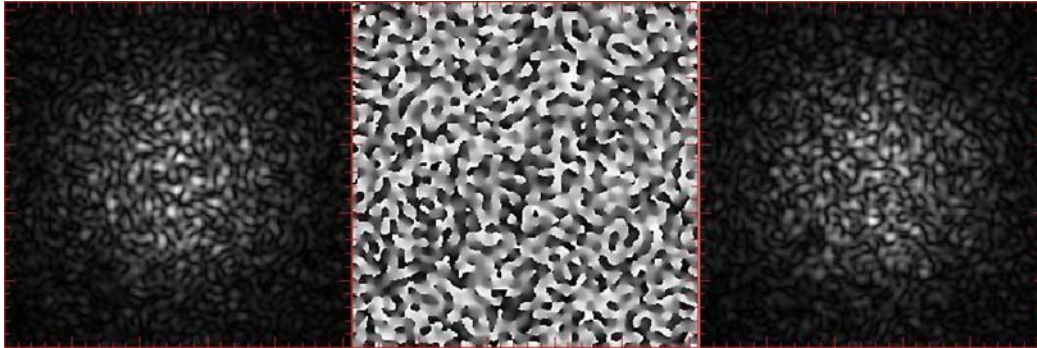


Fig. 10. Simulated input images for testing the phase diversity algorithm.

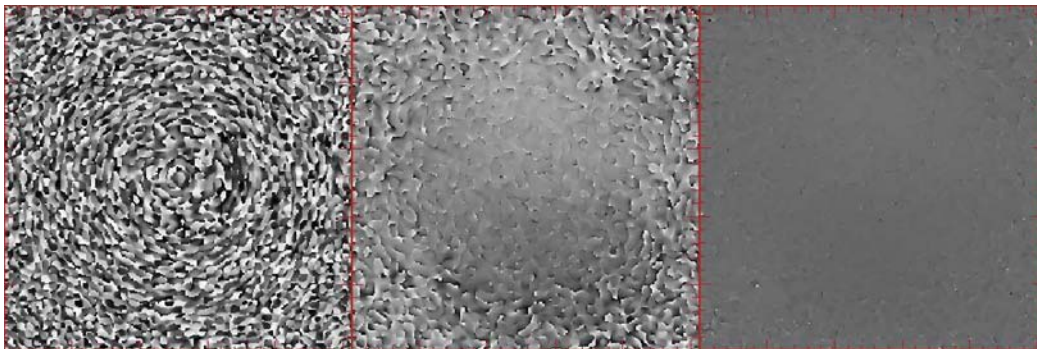


Fig. 11. Differences between the phase in Fig. 10 and the estimated phase after 1, 30, and 60 iterations.

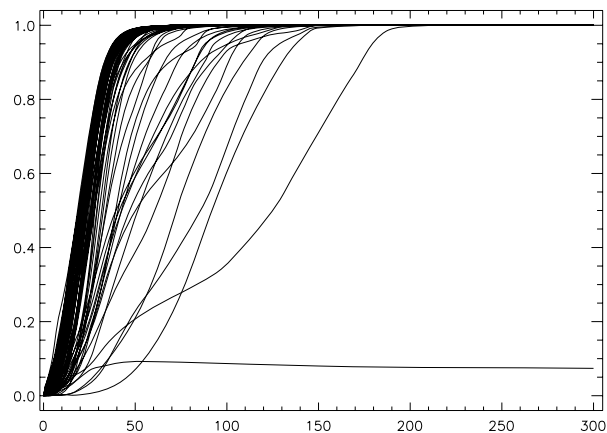


Fig. 12. Spectral Strehl ratio for 100 iterations. Notable are the few slow- and the single non-conversion.

## 7. OUTLOOK

The next steps to get our testbed fully operational are to align the testbed with optimized occulter masks, to implement the single stage Labeyrie speckle correction, to determine the DM response function for the speckle wavefront correction, and to implement the above-described modified Gerchberg-Saxton algorithm into the testbed control software.

## 8. ACKNOWLEDGEMENTS

This work was supported by NASA through grant NNG04GC57G and SAO IR&D funding. The mask development at Harvard University was supported by the Research Experience for Undergraduate Program of the Harvard Materials Science and Engineering Center. Central facilities were provided by Harvard's Center for Nanoscale Systems.

## 9. REFERENCES

1. Tolls, V., Aziz, M., Gonsalves, R.A., Korzennik, S., Labeyrie, A., Lyon, R., Melnick, G., Somerstein, S., Vasudevan, G., Woodruff, R., Techniques and Instrumentation for Detection of Exoplanets II; Daniel R. Coulter, Ed.; Proc. SPIE, Vol. 5905, 2005
2. Kuchner, M.J., and Traub, W.A., ApJ, 570, 900, 2003
3. Kuchner, M.J., Crepp, J., and Ge, J., ApJ, 624, 832, 2005
4. Raja, S.N., priv. communication, 2006
5. Tolls, V., Aziz, M., Gonsalves, R.A., Korzennik, S., Labeyrie, A., Lyon, R., Melnick, G., Somerstein, S., Vasudevan, G., Woodruff, R., Space Telescopes and Instrumentation I: Optical, Infrared, and Millimeter, J.C. Mather, H.A. MacEwen, and M.W.M. de Graauw, Eds.; Proc. SPIE, Vol. 6265, 2006
6. Feit, M.D., and Fleck, Jr., J.A., Appl. Opt., 17, 3990, 1978
7. Lyon, R.G., Hollis, J.M., and Dorband, J.E., ApJ, 478, 658, 1997
8. Gonsalves, R. A. and Tolls, V., in Techniques and Instrumentation for Detection of Exoplanets II; Daniel R. Coulter, Ed.; Proc. SPIE, Vol. 5905, 2005